

## Article

# In Situ Carbon-Confined MoSe<sub>2</sub> Catalyst with Heterojunction for Highly Selective CO<sub>2</sub> Hydrogenation to Methanol

Yanyang Sun, Linfei Xiao \* and Wei Wu \*

National Center for International Research on Catalytic Technology, School of Chemistry and Material Sciences, Heilongjiang University, Harbin 150080, China; sunyanyang99@163.com

\* Correspondence: xiaolf@hlju.edu.cn (L.X.); wuwei@hlju.edu.cn (W.W.)

**Abstract:** The synthesis of methanol from CO<sub>2</sub> hydrogenation is an effective measure to deal with global climate change and an important route for the chemical fixation of CO<sub>2</sub>. In this work, carbon-confined MoSe<sub>2</sub> (MoSe<sub>2</sub>@C) catalysts were prepared by in situ pyrolysis using glucose as a carbon source. The physico-chemical properties and catalytic performance of CO<sub>2</sub> hydrogenation to yield methanol were compared with MoSe<sub>2</sub> and MoSe<sub>2</sub>/C. The results of the structure characterization showed MoSe<sub>2</sub> displayed few layers and a small particle size. Owing to the synergistic effect of the Mo<sub>2</sub>C-MoSe<sub>2</sub> heterojunction and in situ carbon doping, MoSe<sub>2</sub>@C with a suitable C/Mo mole ratio in the precursor showed excellent catalytic performance in the synthesis of methanol from CO<sub>2</sub> hydrogenation. Under the optimal catalyst MoSe<sub>2</sub>@C-55, the selectivity of methanol reached 93.7% at a 9.7% conversion of CO<sub>2</sub> under optimized reaction conditions, and its catalytic performance was maintained without deactivation during a continuous reaction of 100 h. In situ diffuse infrared Fourier transform spectroscopy studies suggested that formate and CO were the key intermediates in CO<sub>2</sub> hydrogenation to methanol.

**Keywords:** MoSe<sub>2</sub>@C; CO<sub>2</sub>; methanol; hydrogenation



**Citation:** Sun, Y.; Xiao, L.; Wu, W. In Situ Carbon-Confined MoSe<sub>2</sub> Catalyst with Heterojunction for Highly Selective CO<sub>2</sub> Hydrogenation to Methanol. *Molecules* **2024**, *29*, 2186. <https://doi.org/10.3390/molecules29102186>

Academic Editor: Jean-Luc Renaud

Received: 11 April 2024

Revised: 29 April 2024

Accepted: 4 May 2024

Published: 8 May 2024



**Copyright:** © 2024 by the authors. Licensee MDPI, Basel, Switzerland. This article is an open access article distributed under the terms and conditions of the Creative Commons Attribution (CC BY) license (<https://creativecommons.org/licenses/by/4.0/>).

## 1. Introduction

A large amount of CO<sub>2</sub> is emitted when extravagant fossil fuels (coal, oil and natural gas) are consumed, which causes a series of climate problems [1,2]. In view of the current situation, in order to reduce CO<sub>2</sub> emissions, carbon capture and storage (CCS) and carbon capture and utilization (CCU) are currently the most effective means [3]. However, the high cost and energy consumption of desorption, compression and storage of captured CO<sub>2</sub> greatly limit the large-scale application of CCS. CCU can achieve efficient CO<sub>2</sub> recovery and bring certain economic benefits, and it is considered a promising technology to reduce CO<sub>2</sub> emissions. As a raw material, CO<sub>2</sub> can be converted to fuel and value-added chemicals [4,5]. On the one hand, it can reduce the pressure of the fossil resource shortage; on the other hand, it can bring huge economic benefits. Therefore, the chemical utilization of CO<sub>2</sub> to produce value-added chemicals has become one of the hot topics for using a non-toxic, inexpensive, abundant and renewable source of carbon [6–9]. Among the CO<sub>2</sub> utilization routes, synthesizing methanol has received extensive attention [10,11]. Methanol is water-soluble, non-toxic, harmless and easy to store and transport, and it is known as the simplest ‘alcohol’, so it has become one of the most important platform compounds in the chemical industry [12]. Methanol can be miscible with water and a variety of organic matter, serving as an alternative clean fuel, liquid organic hydrogen carrier and common organic solvent [12–14]. It can also be used to produce olefins, aromatic hydrocarbons, alkanes and other bulk chemicals [15,16]. At present, the global production of methanol is 110 million metric tons [17].

For the hydrogenation of CO<sub>2</sub> to methanol, the utilization of copper-based catalysts has garnered significant interest. The main active substances of copper-based catalysts in over

60% of related reports are Cu-ZnO composite materials [18]. However, two disadvantages hinder the widespread use of copper-based catalysts. One is that the generation of water in the reaction aggravates the sintering of the active phase, resulting in poor stability of the catalyst, and the other is that the selectivity of methanol is limited due to the reverse water gas reaction [19,20]. Compared with copper-based catalysts, noble metal-based catalysts exhibit excellent stability, anti-sintering and anti-poisoning properties and can be used as an effective alternative to copper-based catalysts. Although noble metal catalysts show a high ability to activate hydrogen and promote hydrogenation, the low selectivity of methanol is yielded due to its weak interaction with CO<sub>2</sub> in the reaction process. Meanwhile, its low abundance and high cost also limit its large-scale application in CO<sub>2</sub> hydrogenation to methanol. Recently, metal oxide catalysts such as In<sub>2</sub>O<sub>3</sub> and Zn-Zr solid solutions have attracted attention [21]. Due to the formation of oxygen vacancies under reaction conditions of 330 °C and 5 MPa, In<sub>2</sub>O<sub>3</sub> provided 100% methanol selectivity in CO<sub>2</sub> hydrogenation, but it could be reduced to In<sup>0</sup> metal, which caused the deactivation during the reaction [22]. Under industrial conditions, the ZnO-ZrO<sub>2</sub> solid solution catalyst demonstrated the capability to facilitate the hydrogenation of CO<sub>2</sub> to methanol [23]. The space-time yield of methanol was as high as 7.75 mol·kg<sup>-1</sup>·h<sup>-1</sup> with an 87.0% selectivity of methanol, and excellent stability was shown in the presence of SO<sub>2</sub> and H<sub>2</sub>S. However, shortcomings are shown in the harsh reaction conditions, poor activity and high energy consumption. Therefore, it is still a challenge to develop highly effective non-precious metal catalysts for CO<sub>2</sub> hydrogenation to form methanol under relatively mild conditions.

Because of their large surface area and large amounts of coordination-unsaturated surface atoms, two-dimensional layered Mo-based catalysts have attracted widespread attention [24,25]. Due to its similar electronic structure to the noble metal Pt, molybdenum carbide displays excellent catalytic performance for hydrogenation and has been applied in hydrodeoxygenation [26,27] and hydrodenitrogenation [28]. In 1992, molybdenum carbide was used as a catalyst for the hydrogenation of CO<sub>2</sub>, resulting in a methanol selectivity of only 17%, with methane and CO being the predominant byproducts [29]. DFT results suggested that enhancing the adsorption of CO<sub>2</sub> on the catalyst surface was beneficial for inhibiting the complete decomposition of CO<sub>2</sub>, thus improving the selectivity of methanol [30]. In our previous work, N,S-doped carbon-confined molybdenum carbide catalysts were synthesized by in situ pyrolysis carbonization [31]. The basic sites generated from N and S in the in situ pyrolysis carbonization increased the adsorption amount of CO<sub>2</sub>. The selectivity of methanol yielded 90% with a CO<sub>2</sub> conversion of 20%. In this catalyst, nano-sized MoS<sub>2</sub> was also generated in the pyrolysis process, which was a key factor in its excellent catalytic performance. On the one hand, in the presence of MoS<sub>2</sub>, CO<sub>2</sub> was adsorbed and dissociated at sulfur vacancies; on the other hand, in-plane sulfur vacancies could inhibit the deep hydrogenation of CO<sub>2</sub> to methane and promote the formation of methanol at low temperatures. More recently, Deng [32] et al. constructed a surface-rich sulfur-vacancy MoS<sub>2</sub> catalyst and applied it for the hydrogenation of CO<sub>2</sub> to form methanol, with the methanol selectivity reaching 94.3% with a CO<sub>2</sub> conversion of 12.5% at 180 °C. MoSe<sub>2</sub>, as a two-dimensional layered material, has stronger metallicity and lower Gibbs free energy than molybdenum sulfide [33], which is more conducive to the adsorption and activation of hydrogen molecules [34]. More importantly, the adsorption capacity of CO<sub>2</sub> is also better than that of MoS<sub>2</sub> [35]. However, MoSe<sub>2</sub> is mainly involved in photocatalysis and electrocatalysis for the hydrogenation of CO<sub>2</sub>, and the main reduction products are methane, carbon monoxide and so on [35]. Qu et al. incorporated K into MoSe<sub>2</sub> and constructed a K-Mo-Se active phase for catalytic syngas conversion to ethanol. By regulating the K/Mo ratio, the proportion of ethanol in the total alcohol reached 58.7% under optimal reaction conditions [36]. To our best knowledge, there is no report on the use of MoSe<sub>2</sub> as a catalyst in the thermocatalytic hydrogenation of CO<sub>2</sub> to produce methanol [37,38]. Therefore, the study of the catalytic behavior of MoSe<sub>2</sub> is significant for the development of non-noble metal catalysts for CO<sub>2</sub> hydrogenation to methanol.

It is well known that, as a typical two-dimensional material, the active sites of MoSe<sub>2</sub> are also mainly located at its edges and defect sites. Therefore, reducing the layer number and particle size of MoSe<sub>2</sub> is an effective route to enhance its catalytic performance. Confined MoSe<sub>2</sub> in carbon materials can effectively prevent the aggregation of MoSe<sub>2</sub> and improve its catalytic performance [39–41]. In this work, MoSe<sub>2</sub> confined by in situ-formed carbon material (MoSe<sub>2</sub>@C) was prepared by introducing glucose as a carbon source into the precursors using the pyrolysis method and applied to CO<sub>2</sub> hydrogenation to form methanol in a fixed-bed reactor. The influences of the preparation conditions and the C/Mo ratio in the precursors on the catalytic performance of MoSe<sub>2</sub>@C were investigated, and the reaction conditions were optimized. Under optimal reaction conditions, a high methanol selectivity of 93.7% was reached. MoSe<sub>2</sub>@C also showed excellent catalytic stability during performance evaluation and could be used for at least 100 h without deactivation.

## 2. Results and Discussion

### 2.1. Catalyst Characterization

#### 2.1.1. Structural Characterizations

Firstly, X-ray powder diffraction was employed to detect the crystal structure of the prepared samples, and the results are shown in Figure 1. The characteristic diffraction peaks of the three samples appeared at  $2\theta = 13.7^\circ, 31.4^\circ, 37.9^\circ, 47.5^\circ, 55.9^\circ, 66.5^\circ$  and  $69.5^\circ$ , corresponding to the (002), (100), (103), (105), (110), (108) and (203) crystal planes of MoSe<sub>2</sub> (PDF 29-0914) [42], and no other diffraction peaks were found. These results indicate that the MoSe<sub>2</sub> crystal phase was prepared. In addition, a slight shift of the (002) crystal plane could be observed, which was attributed to thermal-induced phase segregation [43]. Compared with MoSe<sub>2</sub>, the intensity of the diffraction peaks was weakened, and the half-peak width of the corresponding diffraction peaks increased in the XRD patterns of the MoSe<sub>2</sub>/C sample, indicating that the introduction of a carbon carrier could improve the dispersion of MoSe<sub>2</sub> and inhibit the growth of MoSe<sub>2</sub> particles. Additionally, the characteristic diffraction peaks corresponding to the (002) crystal plane of graphite carbon were also found at  $2\theta = 26^\circ$ . Compared with the XRD patterns of MoSe<sub>2</sub> and MoSe<sub>2</sub>/C, the diffraction peak intensity of MoSe<sub>2</sub>@C-55 was the weakest, the half-peak width was the widest, and the characteristic diffraction peak ( $2\theta = 13.7^\circ$ ) corresponding to the (002) crystal plane of MoSe<sub>2</sub> almost disappeared. These results suggested that the grain size of MoSe<sub>2</sub> was the smallest and the layer number of MoSe<sub>2</sub> was the lowest in MoSe<sub>2</sub>@C-55 compared with MoSe<sub>2</sub> and MoSe<sub>2</sub>/C [44,45]. As a consequence, introducing glucose to the precursor could suppress the growth of MoSe<sub>2</sub> through the confinement of the in situ generation of carbon material in the pyrolysis process. When the C/Mo ratio in the precursor was raised from 15 to 75, MoSe<sub>2</sub>@C-15, MoSe<sub>2</sub>@C-35 and MoSe<sub>2</sub>@C-75 were prepared. Their XRD patterns are shown in Figure S1. The intensity of the diffraction peak corresponding to MoSe<sub>2</sub> gradually declined with the enhancement of the carbon content in the precursor, which means that the confinement of the in situ carbon material improved with the increase in carbon content, and the growth of MoSe<sub>2</sub> particles was repressed, which was beneficial to the dispersion of MoSe<sub>2</sub> in the carbon material.

In order to observe the microstructure and morphology, MoSe<sub>2</sub>/C and MoSe<sub>2</sub>@C-55 were characterized by TEM and HRTEM (Figure 2). The image in Figure 2a shows that MoSe<sub>2</sub> dispersed on the coconut shell carbon, which resulted in the low intensity of the XRD diffraction peak. However, its distribution was not uniform, and agglomeration was observed, which caused MoSe<sub>2</sub> to show larger particles and more layers. In Figure 2b (HRTEM), lattice fringes of 0.28 nm can be observed, which is consistent with the interplanar spacing of the (100) of MoSe<sub>2</sub> [46,47]. Observing the image of MoSe<sub>2</sub>@C-55, as shown in Figure 2c, the agglomeration and accumulation of MoSe<sub>2</sub> particles were effectively inhibited when glucose was introduced to the precursor. This took place because the carbon materials formed from the in situ pyrolysis of glucose showed an inhibitory effect on the growth of MoSe<sub>2</sub> particles, which ensured the high dispersion of MoSe<sub>2</sub>. As a result of it, more active sites were exposed, and its catalytic performance improved. As can also be seen

from the HRTEM image (Figure 2d), a lattice fringe spacing of 0.35 nm was also observed, which belonged to the (004) of MoSe<sub>2</sub>. In addition, a lattice fringe with a spacing of 0.21 nm was also observed (Figure 2d), which was attributed to the (112) of Mo<sub>2</sub>C [48], indicating that Mo<sub>2</sub>C particles were generated during the preparation of MoSe<sub>2</sub>@C-55. Combined with the fact that the corresponding diffraction peaks of Mo<sub>2</sub>C were not observed in the XRD pattern, it can be inferred that the content of Mo<sub>2</sub>C was low and highly dispersed. In addition, the HRTEM images in Figure 2d show that the presence of Mo<sub>2</sub>C interrupted the continuity of MoSe<sub>2</sub>, causing more edge sites of MoSe<sub>2</sub> to expose more active sites [49]. This phenomenon indicated that a MoSe<sub>2</sub>-Mo<sub>2</sub>C heterojunction was generated, which would benefit the synergistic effect of MoSe<sub>2</sub> and Mo<sub>2</sub>C in the catalytic process and improve its catalytic performance [50]. The results in Figure S2a–d show that increasing the content of glucose in the precursor was favorable to improving the dispersion of MoSe<sub>2</sub>, resulting in a gradual decrease in the particle size and layer number of MoSe<sub>2</sub>, which coincided with the characterization results of XRD. The content of glucose in the precursor also affected the exposed crystal planes of MoSe<sub>2</sub> and Mo<sub>2</sub>C. Setting the C/Mo ratio in the precursor at 15 and 35, lattice fringes of 0.28 nm and 0.23 nm (Figure S2e,f) could be observed in the HRTEM images, which were attributed to the (100) of MoSe<sub>2</sub> and the (121) of Mo<sub>2</sub>C [46,47]. However, lattice fringes of 0.26 nm and 0.21 nm assigned to the (102) of MoSe<sub>2</sub> and the (112) of Mo<sub>2</sub>C were observed (Figure S2h) when the C/Mo ratio in the precursor rose to 75 [48]. Owing to the different crystal faces that would display different catalytic performance [49], it can be inferred that there will be a large difference in the catalytic performance of CO<sub>2</sub> hydrogenation to form methanol.

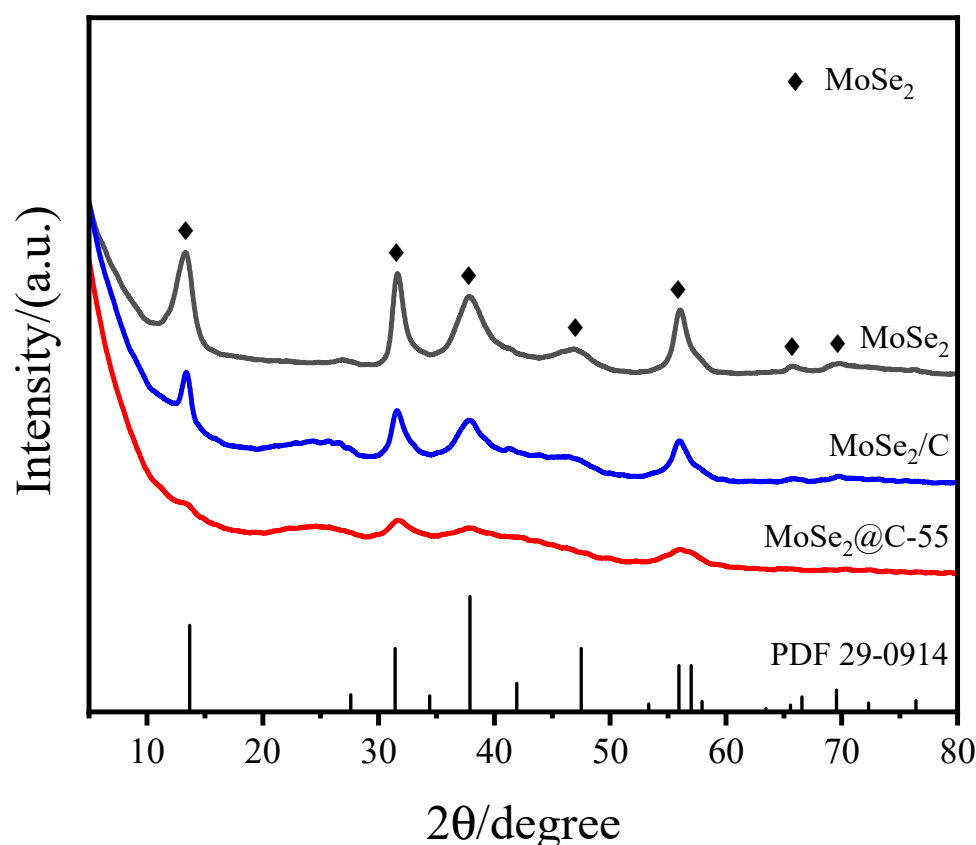
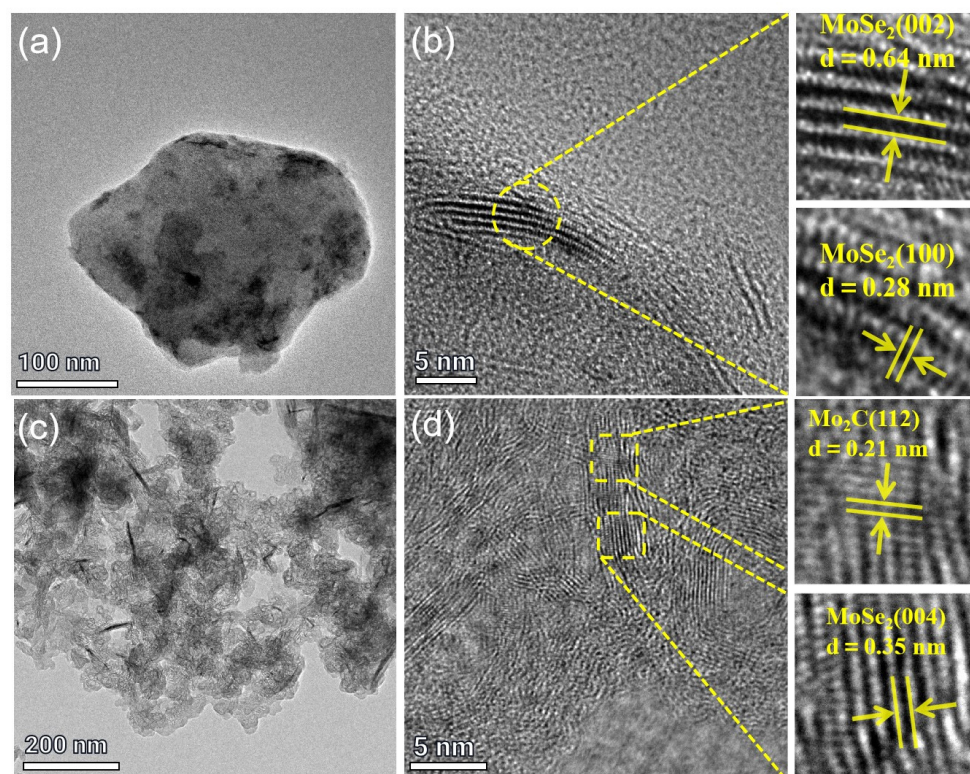


Figure 1. XRD patterns of MoSe<sub>2</sub>, MoSe<sub>2</sub>/C and MoSe<sub>2</sub>@C-55 catalysts.



**Figure 2.** TEM and HRTEM images of MoSe<sub>2</sub>/C and MoSe<sub>2</sub>@C-55 catalysts: (a,b) MoSe<sub>2</sub>/C; (c,d) MoSe<sub>2</sub>@C-55.

### 2.1.2. XPS Analysis of Catalysts

The surface chemical state of the catalyst was further analyzed by XPS. The XPS survey spectra shown in Figure S3 suggest that the surface elements of the samples were Mo, Se, C and O.

The XPS spectra of the Mo 3d of the three samples (Figure 3a and Table S1) showed that characteristic peaks were observed at 229.1–229.3 eV and 232.1–232.3 eV, which were attributed to Mo<sup>4+</sup> 3d<sub>5/2</sub> and 3d<sub>3/2</sub> in MoSe<sub>2</sub> [48,50]. In addition, fitting peaks at 228.6 eV and 231.6 eV were also found in the Mo 3d of MoSe<sub>2</sub>@C-55, which corresponded to Mo<sup>2+</sup> 3d<sub>5/2</sub> and 3d<sub>3/2</sub>, indicating that Mo<sub>2</sub>C was generated during the preparation of MoSe<sub>2</sub>@C-55 [51,52], suggesting that a strong interaction between the carbon formed by the in situ carbonization of glucose and the Mo atoms was formed. The specific binding energy data in Table S1 show that the binding energy of Mo<sup>4+</sup> 3d<sub>5/2</sub> and 3d<sub>3/2</sub> in MoSe<sub>2</sub>@C-55 was 0.2 eV lower than that of MoSe<sub>2</sub> and MoSe<sub>2</sub>/C, which was caused by the electron transfer between MoSe<sub>2</sub> and Mo<sub>2</sub>C [53], and a strong interaction was formed. In addition, peaks at binding energies of 232.5–232.7 eV and 235.4–235.7 eV, corresponding to Mo–O, were observed due to the surface oxidation that took place when MoSe<sub>2</sub>@C-55 and MoSe<sub>2</sub>/C were exposed to air [47–52], but the binding energy of MoSe<sub>2</sub>@C-55 was lower than that of MoSe<sub>2</sub>/C, which may be due to the protective effect of in situ-formed carbon on the surface of MoSe<sub>2</sub>@C-55, resulting in a reduction in the oxidation degree. This result demonstrates once again the robust interaction between carbon and Mo in MoSe<sub>2</sub>@C-55.

The Se 3d XPS spectra are displayed in Figure 3b, and two peaks at 54.7–54.8 eV and 55.7–55.8 eV (Table S2) were assigned to the Se<sup>2-</sup> 3d<sub>5/2</sub> and 3d<sub>3/2</sub> of MoSe<sub>2</sub> [42,46]. Moreover, MoSe<sub>2</sub>/C also showed a characteristic peak at about 59.1 eV, assigned to Se oxide (SeO<sub>x</sub>) [54]. In addition, as shown in Figure 3c and Table S3, the peaks at 284.8 eV and about 286.1 eV in the C 1s spectrum of all samples indicate the formation of a C–C bond and a C–O bond, respectively [55]. The high-resolution XPS spectra of O 1s are shown in Figure 3d and Table S4. The peaks at 530.4 eV, 531.8 eV and 532.8 eV indicate the formation of lattice

oxygen ( $O_{lat}$ ), deficient oxygen ( $O_{def}$ ) and adsorbed oxygen ( $O_{ads}$ ), respectively [56,57]. The proportion of each oxygen species in all oxygen species is shown in Table S4. The proportion of  $O_{def}$  is the highest in the  $MoSe_2@C-55$  catalyst. The oxygen vacancies on the surface improved the dissociation of  $CO_2$  and tended to produce the desired methanol [57]. Moreover, only the  $MoSe_2@C-55$  sample showed a peak at 282.6 eV, which corresponded to a C-Mo bond [53,54]. The data listed in Figure S5 also show that the binding energy of Mo 3d showed a negative shift with the increase in the C/Mo ratio in the precursor, and the  $Mo^{2+}/Mo^{4+}$  ratio on the surface of the catalyst displayed a positive correlation with the carbon content in the precursor (Table S5), suggesting that a higher carbon content in the precursor was beneficial to generating  $Mo_2C$ .

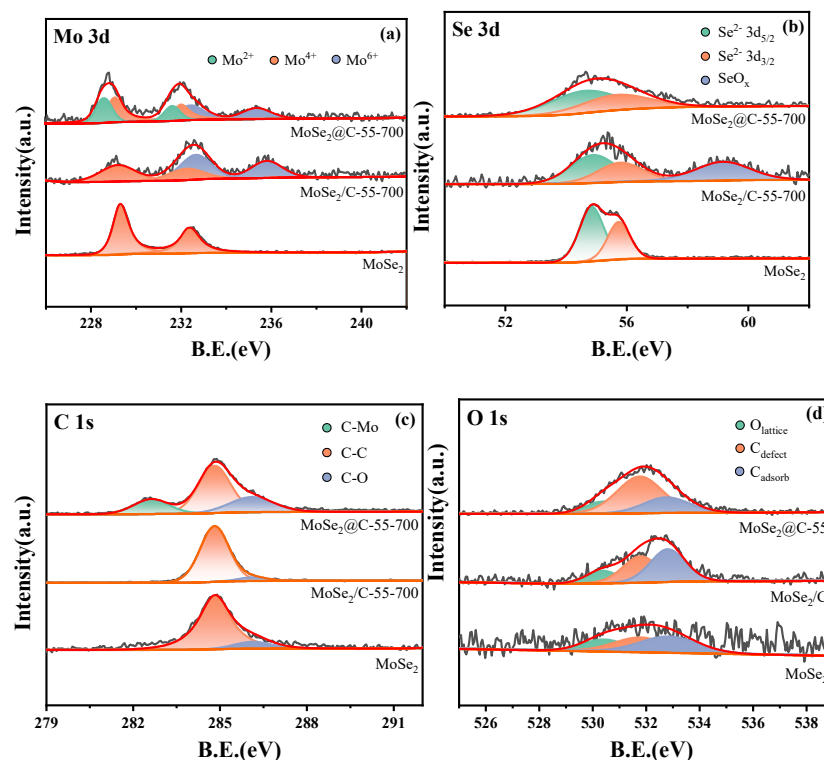


**Figure 3.** XPS spectra of  $MoSe_2$ ,  $MoSe_2/C$  and  $MoSe_2@C$  catalysts: (a) Mo 3d; (b) Se 3d; (c) C 1s; (d) O 1s.

### 2.1.3. Characterization of $CO_2$ Adsorption Capacity

The adsorptive capacity of a catalyst for  $CO_2$  is an important factor in its catalytic performance in  $CO_2$  hydrogenation. Therefore,  $CO_2$ -TPD was carried out, and the desorption curves are displayed in Figure 4. According to the characterization results, all the  $CO_2$  desorption peaks of the prepared  $MoSe_2$ ,  $MoSe_2/C$  and  $MoSe_2@C-55$  catalysts appeared at low temperatures, which corresponded to the presence of weak basic sites on the catalyst surface [58,59]. Compared with  $MoSe_2$  and  $MoSe_2/C$ ,  $MoSe_2@C-55$  showed the highest desorption temperature of  $CO_2$ , which means that the activation degree of  $CO_2$  on the surface of  $MoSe_2@C-55$  was the highest, which would be beneficial to the hydrogenation of  $CO_2$ . Because the magnitude of the peak area corresponds to the quantity of activated  $CO_2$  present on the catalyst surface, the relative desorbed amount of  $CO_2$  was calculated by calculating the area of these peaks, and the results are also inset in Figure 4. Based on the desorption amounts of  $CO_2$  from  $MoSe_2@C-55$  (the relative value is 100%), the desorption amounts of  $CO_2$  from the surface of  $MoSe_2$  and  $MoSe_2/C$  were 45% and 54% (by calculating the area of the  $CO_2$  desorption peak). These results suggest that the order of  $CO_2$  adsorption amounts on the catalyst surface and the ability to activate  $CO_2$  were  $MoSe_2@C-55 > MoSe_2/C > MoSe_2$ .

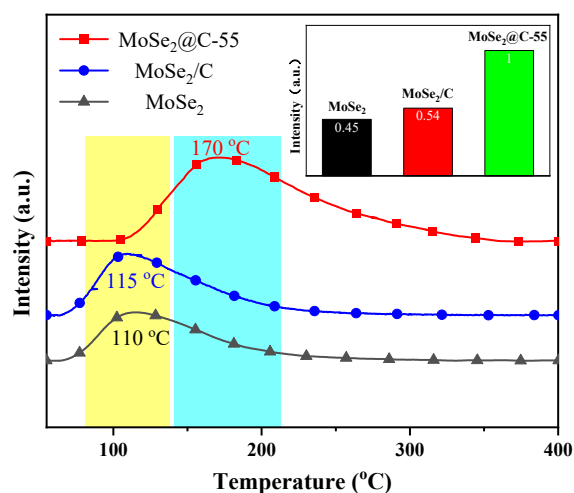


**Figure 4.** CO<sub>2</sub>-TPD profiles of MoSe<sub>2</sub>, MoSe<sub>2</sub>/C and MoSe<sub>2</sub>@C-55 catalysts.

## 2.2. Catalytic Performance in CO<sub>2</sub> Hydrogenation to Yield Methanol

In a fixed-bed reactor at 180 °C, 3MPa and a Gas Hourly Space Velocity (GHSV) of 3000 mL·g<sub>cat</sub><sup>-1</sup>·h<sup>-1</sup>, the catalytic performance of MoSe<sub>2</sub>, MoSe<sub>2</sub>/C and MoSe<sub>2</sub>@C-55 was evaluated for CO<sub>2</sub> hydrogenation to yield methanol (Table 1). In the presence of the MoSe<sub>2</sub> catalyst, the conversion of CO<sub>2</sub> was as low as 2.4%, and only a moderate selectivity (52.5%) of methanol was observed in the hydrogenation process, while CO was yielded with a selectivity of 33.1%. In this process, CO was generated from the reverse water gas shift (RWGS) reaction of CO<sub>2</sub> on the surface of MoSe<sub>2</sub>, which was an important intermediate for synthesizing methanol. However, the insufficient active sites were exposed and could not achieve further efficient CO conversion, resulting in high CO selectivity [60]. At the same time, the CH<sub>3</sub>O\* intermediate generated by CO hydrogenation was more likely to undergo C-O cleavage to generate CH<sub>3</sub>\* and OH\* at the active sites, resulting in a high CH<sub>4</sub> selectivity (10.2%) [32]. In addition, a small amount of dimethyl ether was generated by further dehydration of methanol, which was due to the weak acidity generated from the oxidation of the surface of MoSe<sub>2</sub> [61]. The selectivity of methanol increased to 89.9% at a CO<sub>2</sub> conversion of 4.3% over the MoSe<sub>2</sub>/C catalyst, prepared by using coconut shell carbon as support. This was attributed to an increase in the dispersion of MoSe<sub>2</sub> on the support, which was beneficial for exposing more edge sites and surface defects due to the reduction in the particle size and layer number of MoSe<sub>2</sub> [32]. The conversion of CO<sub>2</sub> increased to 9.7% by employing MoSe<sub>2</sub>@C-55 as a catalyst prepared by using glucose as a carbon source with a C/Mo ratio of 55, while the selectivity of methanol further increased to 93.7% and the selectivity of CH<sub>4</sub> decreased to 6.3%, which can be explained by the following reasons: On the one hand, the in situ-formed carbon gave a strong confinement to MoSe<sub>2</sub>, resulting in a decreasing layer number, which could expose more surface defects conducive to methanol generation. Moreover, the highest amount of deficient oxygen was detected by XPS, and the oxygen vacancies on the surface improved the dissociation of CO<sub>2</sub> and tended to produce the desired methanol [57]. On the other hand, in situ-generated Mo<sub>2</sub>C interrupted the continuity of MoSe<sub>2</sub>, and the MoSe<sub>2</sub>-Mo<sub>2</sub>C heterojunction was formed, which was beneficial for exposing more active sites and activating H<sub>2</sub> (Figure S5). The above factors all led to improved CO<sub>2</sub> conversion and selectivity of methanol in CO<sub>2</sub> hydrogenation. Moreover, the high desorption capacity and the high CO<sub>2</sub> activation ability of MoSe<sub>2</sub>@C-55 were also important factors for increasing CO<sub>2</sub> conversion. Based on the above research results, the catalytic performances of a series of MoSe<sub>2</sub>@C-x (x = 15, 35 and 75) catalysts with different C/Mo ratios in the precursors were also evaluated (Table 1). It can be seen that the selectivity of methanol gradually increased with the increase in C/Mo ratios. When MoSe<sub>2</sub>@C-75 was used as the catalyst, the selectivity of methanol reached a maximum of 94.3%. This was due to the fact that the number of layers of MoSe<sub>2</sub> was

reduced as the carbon content in the precursors increased, which was favorable for the exposure of surface defects and conducive to the formation of methanol. The conversion of CO<sub>2</sub> reached its maximum when MoSe<sub>2</sub>@C-55 was used as the catalyst. This took place because MoSe<sub>2</sub>@C-55 had a stronger ability to adsorb and activate CO<sub>2</sub> (Figure S6), causing an acceleration of CO<sub>2</sub> conversion.

**Table 1.** Results of CO<sub>2</sub> hydrogenation to methanol over different catalysts <sup>a</sup>.

| Catalyst                | Conversion (%) | Selectivity (%)    |                 |      |                                  |
|-------------------------|----------------|--------------------|-----------------|------|----------------------------------|
|                         |                | CH <sub>3</sub> OH | CH <sub>4</sub> | CO   | CH <sub>3</sub> OCH <sub>3</sub> |
| MoSe <sub>2</sub>       | 2.4            | 52.5               | 10.2            | 33.1 | 4.2                              |
| MoSe <sub>2</sub> /C    | 4.3            | 89.9               | 10.1            | -    | -                                |
| MoSe <sub>2</sub> @C-55 | 9.7            | 93.7               | 6.3             | -    | -                                |
| MoSe <sub>2</sub> @C-15 | 2.8            | 72.3               | 27.7            | -    | -                                |
| MoSe <sub>2</sub> @C-35 | 3.3            | 89.5               | 10.5            | -    | -                                |
| MoSe <sub>2</sub> @C-75 | 4.4            | 94.3               | 5.7             | -    | -                                |

<sup>a</sup> Reaction conditions: 180 °C, 3 MPa, GHSV 3000 mL·g<sub>cat</sub><sup>-1</sup>·h<sup>-1</sup>, H<sub>2</sub>:CO<sub>2</sub> = 3.

Compared with the Cu/In<sub>2</sub>O<sub>3</sub>-, CuZnAl- and MoS<sub>2</sub>-based catalysts in the literature, MoSe<sub>2</sub>@C-55 showed better selectivity for methanol under low reaction temperatures, as shown in Table S7.

In CO<sub>2</sub> hydrogenation, CO<sub>2</sub> conversion and methanol selectivity were sensitive to the reaction temperature. Using MoSe<sub>2</sub>@C-55 as a catalyst, the effect of the reaction temperature was investigated under conditions of 3 MPa and a GHSV of 3000 mL·g<sub>cat</sub><sup>-1</sup>·h<sup>-1</sup> (Figure 5a). The results in Figure 5a show that the conversion of CO<sub>2</sub> increased from 7.1% to 13.5% as the reaction temperature rose from 160 °C to 240 °C, suggesting that high temperatures are beneficial for CO<sub>2</sub> to overcome the limitation of its thermodynamic stability, which accelerated the conversion rate of CO<sub>2</sub> [62,63]. Setting the reaction temperature at 180 °C, the selectivity of methanol reached a maximum of 93.7% and gradually decreased as the reaction temperature increased. This took place because the reaction of CO<sub>2</sub> hydrogenation to methanol was an exothermic reaction, and a higher temperature was not conducive to the formation of methanol. Since the reverse water gas reaction is an endothermic reaction [60], high temperatures are beneficial to its occurrence. Therefore, CO was not detected as a byproduct when the reaction temperature was not higher than 220 °C. But 1.5% of CO and 33.6% of CH<sub>4</sub> were generated by raising the reaction temperature to 240 °C. As shown in Figure 5b, the influence of reaction pressure on the hydrogenation of CO<sub>2</sub> was also investigated. The conversion of CO<sub>2</sub> and the selectivity of methanol were all preferential to enhancing reaction pressure. When the reaction pressure was 2 MPa, CO<sub>2</sub> conversion and methanol selectivity were both at a low level (5.6% and 90.6%, respectively). Moreover, the selectivity of methanol improved from 90.6 to 93.7% by changing the reaction pressure from 2 MPa to 3 MPa. When the reaction pressure was further increased, the selectivity of methanol did not change significantly. Finally, the effects of the space–time rate were also investigated (Figure 5c). With the increase in the space–time rate, the residence time of the feed gas on the surface of MoSe<sub>2</sub>@C-55 was shortened, resulting in a reduction in the conversion of CO<sub>2</sub>. When the space velocity was 3000 mL·g<sub>cat</sub><sup>-1</sup>·h<sup>-1</sup>, the highest methanol selectivity at a moderate CO<sub>2</sub> conversion was obtained. Under optimized reaction conditions, the test of the catalytic stability of the MoSe<sub>2</sub>@C-55 catalyst was performed, and the results are shown in Figure 5d. It indicated that the MoSe<sub>2</sub>@C-55 catalyst could be used continuously for at least 100 h without reducing catalytic activity and showing excellent catalytic stability. The selectivity of methanol was maintained at about 93.7% at a CO<sub>2</sub> conversion of approximately 9.7%.

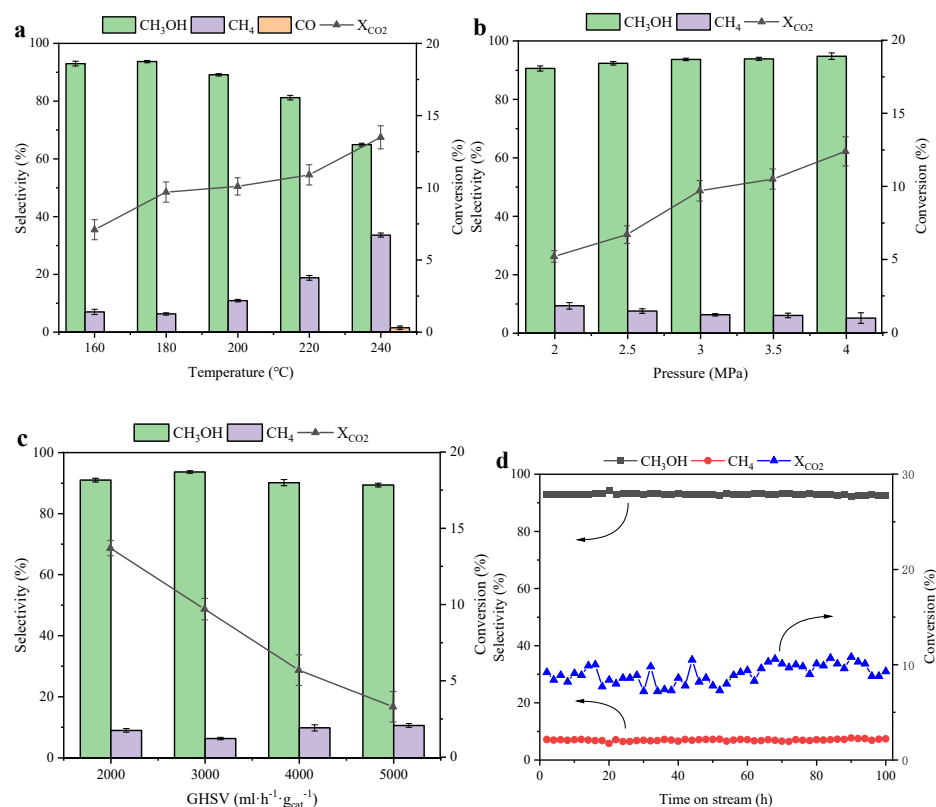


**Figure 5.** Catalytic performance of hydrogenation of CO<sub>2</sub> over MoSe<sub>2</sub>@C-55 under different conditions: (a) effect of temperature; (b) effect of pressure; (c) effect of space velocity; (d) stability evaluation.

### 2.3. Reaction Mechanism

In order to explore the reaction mechanism of the hydrogenation of CO<sub>2</sub> to generate methanol over the MoSe<sub>2</sub>@C-55 catalyst, the possible intermediates on the surface of MoSe<sub>2</sub>@C-55 were detected by in situ diffuse reflectance infrared Fourier transform spectroscopy (DRIFTS). Firstly, the catalyst was activated at 400 °C for 1 h in a pure H<sub>2</sub> atmosphere and then refrigerated to 180 °C. Figure 6 shows the experimental results of the CO<sub>2</sub> hydrogenation reaction stage at atmospheric pressure and a reaction temperature of 180 °C.

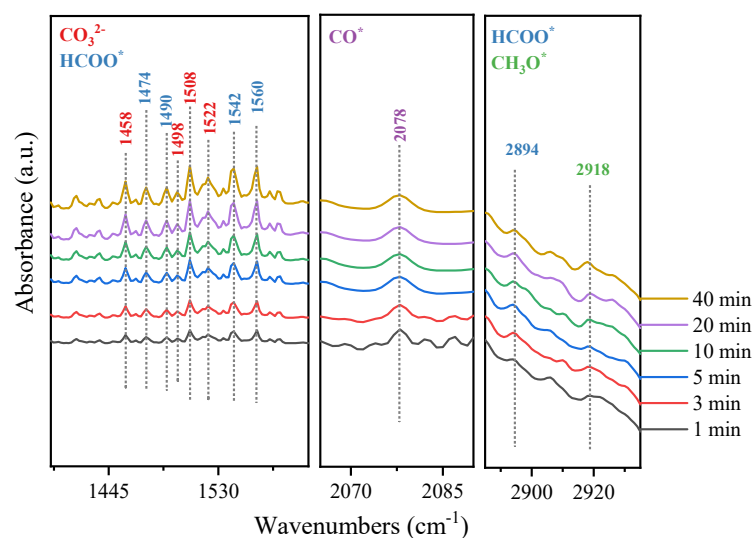
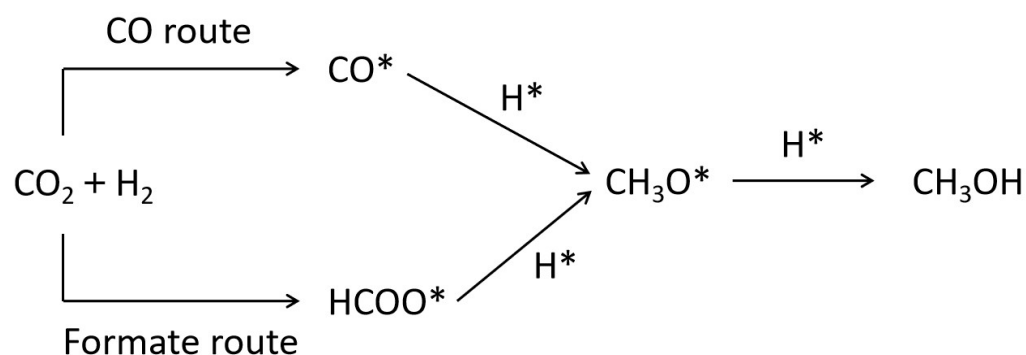


**Figure 6.** DRIFTS spectra of CO<sub>2</sub> hydrogenation in the presence of MoSe<sub>2</sub>@C-55.

From the in situ DRIFTS, two peaks were observed at 1458 and 1522  $\text{cm}^{-1}$ , corresponding to carbonate species ( $\text{CO}_3^{2-}$ ) [64,65]. In addition, two peaks at 1498 and 1508  $\text{cm}^{-1}$  were also observed, corresponding to monodentate and bidentate carbonate species [66], and their intensity gradually increased with the prolongation of the reaction time. As a result of these,  $\text{CO}_2$  first adsorbed on the surface of  $\text{MoSe}_2@\text{C-55}$  and then converted into a carbonate ( $\text{CO}_3^{2-}$ ) species. The C-H bond vibration of the formate species at 1490  $\text{cm}^{-1}$  [67] and spectral bands at 1560, 1542, 1474 and 2894  $\text{cm}^{-1}$  could be observed, corresponding to the symmetric OCO stretching vibration and the stretching vibration of the formate species [68–71]. In addition, the characteristic absorption peak at 2918  $\text{cm}^{-1}$  was attributed to the vibration of the C-H bond of the  $\text{CH}_3\text{O}^*$  species [72]. The above results indicated that there may be a reaction path in the reaction process from  $\text{CO}_2$  hydrogenation to  $\text{HCOO}^*$  species and finally to  $\text{CH}_3\text{OH}$ . Specifically, the adsorbed  $\text{CO}_2$  was converted to carbonate, then  $\text{HCOO}^*$  species were generated from the reaction between carbonate and hydrogen, and  $\text{CH}_3\text{O}^*$  was formed from the hydrogenation of the  $\text{HCOO}^*$  species. Subsequently,  $\text{CH}_3\text{O}^* \rightarrow \text{CH}_3\text{OH}^* \rightarrow \text{CH}_3\text{OH}(\text{g})$  were performed. At the same time, a characteristic peak was observed at 2078  $\text{cm}^{-1}$ , attributed to  $\text{CO}^*$  [69], which provided evidence for the dissociation of  $\text{CO}_2$  when it was adsorbed on the catalyst surface. However,  $\text{CO}$  was not detected in the reaction products when the reaction was carried out at 180  $^\circ\text{C}$ , suggesting that the hydrogenation of  $\text{CO}$  occurred. Therefore, there is another reaction path in  $\text{CO}_2$  hydrogenation over the  $\text{MoSe}_2@\text{C-55}$  catalyst, where the adsorbed  $\text{CO}_2$  is dissociated to  $\text{CO}$ , which is then directly hydrogenated to  $\text{CH}_3\text{O}^*$  and finally to  $\text{CH}_3\text{OH}$ . The detailed reaction pathway is shown in Scheme 1.



**Scheme 1.** Supposed reaction path of  $\text{CO}_2$  hydrogenation to methanol in the presence of  $\text{MoSe}_2@\text{C-55}$ .

### 3. Experiment

#### 3.1. Materials

Ammonium molybdate ( $(\text{NH}_4)_6\text{Mo}_7\text{O}_{24} \cdot 4\text{H}_2\text{O}$ , AMT) and glucose were obtained from Tianjin Kemiou Chemical Reagents Co., Ltd. (Tianjin, China). Selenium powder was purchased from MackLin Chemical Reagents Co., Ltd. (Shanghai, China), and sodium borohydride was obtained from Tianjin Kemiou Chemical Reagents Co., Ltd. (Tianjin, China).  $\text{H}_2$  (99.99%),  $\text{N}_2$  (99.99%),  $\text{CO}_2$  (99.99%) and 5% Ar/95%  $\text{H}_2$  (99.99%) were bought from Qinghua Gas Co., Ltd. (Harbin, China). Without further purification, all reagents were used directly.

#### 3.2. Preparation of Catalysts

##### 3.2.1. Preparing the $\text{MoSe}_2@\text{C-55}$ Catalyst

Ammonium molybdate (0.4022 g) and glucose (4.1381 g) ( $n(\text{C})/n(\text{Mo}) = 55$ ) were dissolved in deionized water. After removal of the water, the prepared product was dried at 110  $^\circ\text{C}$  for 12 h. Subsequently, it was mixed with selenium powder (0.3598 g) and placed in a tubular furnace. In a  $\text{N}_2$  atmosphere, the temperature was increased to 700  $^\circ\text{C}$  at a rate of 5  $^\circ\text{C}/\text{min}$  for 4 h, and  $\text{MoSe}_2$  confined in carbon material catalyst ( $\text{MoSe}_2@\text{C-55}$ , where 55 is the carbon–molybdenum ratio (C/Mo) in the precursor) was obtained. When

the C/Mo ratio in the precursors changed to 15, 35 and 75, they were named MoSe<sub>2</sub>@-15, MoSe<sub>2</sub>@-35 and MoSe<sub>2</sub>@-75, respectively.

### 3.2.2. Preparing the MoSe<sub>2</sub>/C Catalyst

A total of 0.4022 g ammonium molybdate was impregnated into 1.5036 g coconut shell carbon by the impregnation method and dried at 110 °C overnight. After mixing the dried solid and 0.3598 g selenium powder, the resulting products were roasted in a tube furnace. In a H<sub>2</sub>/N<sub>2</sub> atmosphere containing 30% H<sub>2</sub>, the temperature was raised to 700 °C at 5 °C/min for 4 h. The MoSe<sub>2</sub>/C sample was obtained.

### 3.2.3. Preparing the MoSe<sub>2</sub> Catalyst

An aqueous solution containing sodium borohydride (0.3972 g) was added drop by drop to 0.5527 g selenium powder, and the mixture was stirred to form a reddish-brown solution at 70 °C. Then, the reddish-brown mixture was added to an aqueous solution containing ammonium molybdate (0.6180 g). After stirring at ambient temperature for 30 min, the mixture was put into a 50 mL stainless steel autoclave lined with PTFE and crystallized at 220 °C for 24 h, then cooled to ambient temperature. Subsequently, it was centrifuged, washed, dried and put into a tubular furnace. In a N<sub>2</sub> atmosphere, the temperature of the tubular furnace rose to 550 °C at a rate of 5 °C/min, and it was held for 2 h. Then, it was refrigerated to ambient temperature, and the MoSe<sub>2</sub> sample was obtained.

### 3.3. Characterization

X-ray powder diffraction (XRD, Bruker D8, Advance, Salbrücken, Germany) of Cu-K $\alpha$  radiation diffraction (019B = 1.5406Å) was used to characterize the crystal structure of the samples, and transmission electron microscopy (TEM, JEM-2100, Tokyo, Japan) and high-resolution transmission electron microscopy (HRTEM, JEM-2100, Tokyo, Japan) were used to observe their morphology and size. An X-ray photoelectron spectrometer (ESCALAB 250-11 OOV, Thermo Fisher, Waltham, MA, USA) was employed to determine the types and valence of the elements on their surface. CO<sub>2</sub> temperature-programmed desorption (TPD) was carried out on a chemisorption instrument equipped with a thermal conductivity detector (TCD). The process was as follows: After pretreatment at 500 °C for 60 min in Ar (40 mL/min), the sample (0.2 g) was exposed to CO<sub>2</sub> (40 mL/min) for 60 min while it was cooled to 50 °C. Subsequently, the physically adsorbed CO<sub>2</sub> was eliminated in a pure Ar (40 mL/min) atmosphere for 60 min. Then, the desorption of CO<sub>2</sub> was measured from 50 °C to 500 °C at a rate of 10 °C/min in an Ar (40 mL/min) atmosphere. On a Perkin Elmer frontier spectrometer (Waltham, MA, USA), in situ diffuse infrared Fourier transform spectroscopy (DRIFTS) measurements were carried out. Firstly, the sample was pretreated at 400 °C for 60 min with a H<sub>2</sub> flow of 30 mL/min and then chilled to 180 °C. Subsequently, gas feed (H<sub>2</sub> 30 mL/min and CO<sub>2</sub> 10 mL/min) was introduced after scanning the background spectrum in the range of 400–4000 cm<sup>-1</sup>, and the samples were scanned four times in the first 10 min and twice in 30 min.

### 3.4. Catalytic Performance Evaluation

The hydrogenation of CO<sub>2</sub> to yield methanol was performed in a fixed-bed reactor (inner diameter of 6 mm). The schematic diagram of the reaction device is shown in Figure 7. After the catalyst (0.5 g) was pretreated in pure H<sub>2</sub> at 400 °C for 3 h and chilled to 180 °C, the feed gas (H<sub>2</sub>/CO<sub>2</sub> ratio of 3/1) was introduced into the reactor under 3.0 MPa. The reaction tail gas was quantitatively analyzed using a gas chromatograph equipped with a hydrogen flame detector (GC-7900, Tianmei, Shanghai, China) and a thermal conductivity detector (GC-7890II, Tianmei, Shanghai, China).

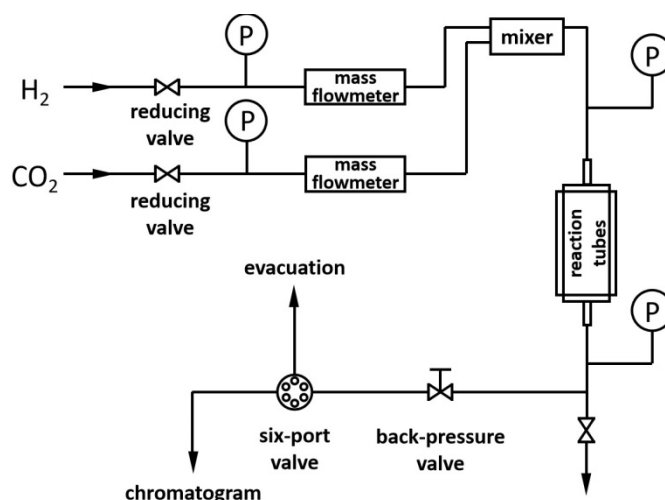


Figure 7. Schematic diagram of the reaction device.

#### 4. Conclusions

MoSe<sub>2</sub> catalysts were prepared by different loading methods and applied to carry out the hydrogenation of CO<sub>2</sub> to methanol. The introduction of carbon materials can effectively improve the dispersion of MoSe<sub>2</sub>. When glucose was introduced into the precursor as a carbon source, small particles and a few layers of MoSe<sub>2</sub> were formed in the MoSe<sub>2</sub>@C-55 catalyst under the confinement of the in situ-formed carbon material, which was beneficial for exposing more active sites.

Due to the strong interaction between MoSe<sub>2</sub> and the in situ-formed carbon, the MoSe<sub>2</sub>-Mo<sub>2</sub>C heterojunction was generated, which interrupted the continuity of MoSe<sub>2</sub>. Under the confinement effect of the in situ-formed carbon material, the layer number and particle size of MoSe<sub>2</sub> were reduced in the MoSe<sub>2</sub>@C-55 catalyst, which was conducive to exposing more active sites.

Over the MoSe<sub>2</sub>@C-55 catalyst, a higher methanol selectivity of 93.7% and excellent catalytic stability in the continuous reaction within 100 h provide a prospect for the application of the high-efficiency catalyst under the cooperation of the MoSe<sub>2</sub>-Mo<sub>2</sub>C heterojunction and the in situ-formed carbon material. The results of the in situ DRIFTS proved the HCOO\* and CO\* species were the intermediates for synthesizing methanol from CO<sub>2</sub> in the presence of a MoSe<sub>2</sub>@C-55 catalyst.

**Supplementary Materials:** The following supporting information can be downloaded at <https://www.mdpi.com/article/10.3390/molecules29102186/s1>: Figure S1. XRD patterns of MoSe<sub>2</sub>@C-x catalysts prepared with different C/Mo ratios; Figure S2. TEM and HRTEM images of MoSe<sub>2</sub>@C-x catalysts prepared with different C/Mo ratios: (a,e) MoSe<sub>2</sub>@C-15; (b,f) MoSe<sub>2</sub>@C-35; (c,g) MoSe<sub>2</sub>@C-55; (d,h) MoSe<sub>2</sub>@C-75; Figure S3. Survey XPS spectra of MoSe<sub>2</sub>, MoSe<sub>2</sub>/C and MoSe<sub>2</sub>@C catalysts; Figure S4. XPS spectra of MoSe<sub>2</sub>@C-x catalysts prepared with different C/Mo ratios: (a) survey spectrum; (b) Mo 3d; (c) Se 3d; (d) C 1s; (e) O 1s; Figure S5. Activating H<sub>2</sub> on the MoSe<sub>2</sub>-Mo<sub>2</sub>C heterojunction; Figure S6. CO<sub>2</sub>-TPD of MoSe<sub>2</sub>@C-x with different C/Mo ratios; Table S1. The valence state and distribution of the Mo element on the surface of the MoSe<sub>2</sub>, MoSe<sub>2</sub>/C and MoSe<sub>2</sub>@C catalysts; Table S2. The valence state and distribution of the Se element on the surface of the MoSe<sub>2</sub>, MoSe<sub>2</sub>/C and MoSe<sub>2</sub>@C catalysts; Table S3. The valence state and distribution of the C element on the surface of the MoSe<sub>2</sub>, MoSe<sub>2</sub>/C and MoSe<sub>2</sub>@C catalysts; Table S4. The valence state and distribution of the O element on the surface of the MoSe<sub>2</sub>, MoSe<sub>2</sub>/C and MoSe<sub>2</sub>@C catalysts; Table S5. The valence state and distribution of the Mo element on the surface of MoSe<sub>2</sub>@C-x; Table S6. The valence state and distribution of the O element on the surface of MoSe<sub>2</sub>@C-x; Table S7. Comparison between MoSe<sub>2</sub>@C-55 and reported catalysts in CO<sub>2</sub> hydrogenation to methanol [73–77].

**Author Contributions:** Y.S.: Experimental operation, Data curation, Writing—original draft. L.X.: Supervision, Writing—review and editing, Project administration. W.W.: Supervision, Writing—review and editing, Project administration. All authors have read and agreed to the published version of the manuscript.

**Funding:** This research was funded by Basal Research Fund of Provincial Higher Education Institutions in Heilongjiang Province (2022-KYYWF-1061).

**Institutional Review Board Statement:** Not applicable.

**Informed Consent Statement:** Not applicable.

**Data Availability Statement:** All data generated or analyzed during this study are included in this published article.

**Conflicts of Interest:** The authors declare no conflicts of interest.

## References

1. Zhong, S.; Guo, X.; Zhou, A.; Chen, Z.; Jin, D.; Fan, M.; Ma, T. Fundamentals and recent progress in magnetic field assisted CO<sub>2</sub> capture and conversion. *Small* **2024**, *20*, 2305533. [[CrossRef](#)] [[PubMed](#)]
2. Wang, Q.; Luo, J.; Zhong, Z.; Borgna, A. CO<sub>2</sub> capture by solid adsorbents and their applications: Current status and new trends. *Energy Environ. Sci.* **2011**, *4*, 42–55. [[CrossRef](#)]
3. MacDowell, N.; Florin, N.; Buchard, A.; Hallett, J.; Galindo, A.; Jackson, G.; Adjiman, C.S.; Williams, C.K.; Shah, N.; Fennell, P. An overview of CO<sub>2</sub> capture technologies. *Energy Environ. Sci.* **2010**, *3*, 1645–1669. [[CrossRef](#)]
4. Zhang, Y.; Zhao, S.; Li, L.; Feng, J.; Li, K.; Lin, H. Integrated CO<sub>2</sub> capture and utilization: A review of the synergistic effects of dual function materials. *Catal. Sci. Technol.* **2024**, *14*, 790–819. [[CrossRef](#)]
5. Zhang, X.G.; Buthiyappan, A.; Jewaratnam, J.; Metselaar, H.S.C.; Raman, A.A.A. Bifunctional materials for integrated CO<sub>2</sub> capture and conversion: Review on adsorbent and catalyst types, recent advances, and challenges. *J. Environ. Chem. Eng.* **2024**, *12*, 111799. [[CrossRef](#)]
6. Zhang, Z.; Pan, S.-Y.; Li, H.; Cai, J.; Olabi, A.G.; Anthony, E.J.; Manovic, V. Recent advances in carbon dioxide utilization. *Renew. Sustain. Energy Rev.* **2020**, *125*, 109799. [[CrossRef](#)]
7. Al-Rowaili, F.N.; Zahid, U.; Onaizi, S.; Khaled, M.; Jamal, A.; AL-Mutairi, E.M. A review for Metal-Organic Frameworks (MOFs) utilization in capture and conversion of carbon dioxide into valuable products. *J. CO<sub>2</sub> Util.* **2021**, *53*, 101715. [[CrossRef](#)]
8. Chen, S.; Liu, J.; Zhang, Q.; Teng, F.; McLellan, B.C. A critical review on deployment planning and risk analysis of carbon capture, utilization, and storage (CCUS) toward carbon neutrality. *Renew. Sustain. Energy Rev.* **2022**, *167*, 112537. [[CrossRef](#)]
9. Liu, J.; Song, Y.; Guo, X.; Song, C.; Guo, X. Recent advances in application of iron-based catalysts for CO<sub>x</sub> hydrogenation to value-added hydrocarbons. *Chin. J. Catal.* **2022**, *43*, 731–754. [[CrossRef](#)]
10. Navarro-Jaén, S.; Virginie, M.; Bonin, J.; Robert, M.; Wojcieszak, R.; Khodakov, A.Y. Highlights and challenges in the selective reduction of carbon dioxide to methanol. *Nat. Rev. Chem.* **2021**, *5*, 564–579. [[CrossRef](#)]
11. Jiang, X.; Nie, X.; Guo, X.; Song, C.; Chen, J.G. Recent advances in carbon dioxide hydrogenation to methanol via heterogeneous catalysis. *Chem. Rev.* **2020**, *120*, 7984–8034. [[CrossRef](#)]
12. Sen, R.; Goepfert, A.; Prakash, G.K.S. Homogeneous hydrogenation of CO<sub>2</sub> and CO to methanol: The renaissance of low-temperature catalysis in the context of the methanol economy. *Angew. Chem. Int. Ed.* **2022**, *61*, e202207278. [[CrossRef](#)] [[PubMed](#)]
13. Deka, T.J.; Osman, A.I.; Baruah, D.C.; Rooney, D.W. Methanol fuel production, utilization, and techno-economy: A review. *Environ. Chem. Lett.* **2022**, *20*, 3525–3554. [[CrossRef](#)]
14. Onishi, N.; Himeda, Y. Homogeneous catalysts for CO<sub>2</sub> hydrogenation to methanol and methanol dehydrogenation to hydrogen generation. *Coord. Chem. Rev.* **2022**, *472*, 214767. [[CrossRef](#)]
15. Sheetal; Mehara, P.; Das, P. Methanol as a greener C1 synthon under non-noble transition metal-catalyzed conditions. *Coord. Chem. Rev.* **2023**, *475*, 214851. [[CrossRef](#)]
16. Bowker, M. Methanol synthesis from CO<sub>2</sub> hydrogenation. *ChemCatChem* **2019**, *11*, 4238–4246. [[CrossRef](#)] [[PubMed](#)]
17. LBobadilla, F.; Azancot, L.; González-Castaño, M.; Ruiz-López, E.; Pastor-Pérez, L.; Durán-Olivencia, F.-J.; Odriozola, J.-A. Biomass gasification, catalytic technologies and energy integration for production of circular methanol: New horizons for industry decarbonisation. *J. Environ. Sci.* **2024**, *140*, 306–318. [[CrossRef](#)] [[PubMed](#)]
18. Qi, S.C.; Liu, X.Y.; Zhu, R.R.; Xue, D.M.; Liu, X.Q.; Sun, L.B. Causation of catalytic activity of Cu-ZnO for CO<sub>2</sub> hydrogenation to methanol. *Chem. Eng. J.* **2022**, *430*, 132784. [[CrossRef](#)]
19. Qi, T.; Li, W.; Li, H.; Ji, K.; Chen, S.; Zhang, Y. Ytria-doped Cu/ZnO catalyst with excellent performance for CO<sub>2</sub> hydrogenation to methanol. *Mol. Catal.* **2021**, *509*, 111641. [[CrossRef](#)]
20. Guo, H.; Li, Q.; Zhang, H.; Peng, F.; Xiong, L.; Yao, S.; Huang, C.; Chen, X. CO<sub>2</sub> hydrogenation over acid-activated Attapulgitite/Ce<sub>0.75</sub>Zr<sub>0.25</sub>O<sub>2</sub> nanocomposite supported Cu-ZnO based catalysts. *Mol. Catal.* **2019**, *476*, 110499. [[CrossRef](#)]

21. Sha, F.; Han, Z.; Tang, S.; Wang, J.; Li, C. Hydrogenation of carbon dioxide to methanol over Non-Cu-based heterogeneous catalysts. *ChemSusChem* **2020**, *13*, 6160–6181. [[CrossRef](#)] [[PubMed](#)]
22. Martín, O.; Martín, A.J.; Mondelli, C.; Mitchell, S.; Segawa, T.F.; Hauert, R.; Drouilly, C.; Curulla-Ferré, D.; Pérez-Ramírez, J. Indium oxide as a superior catalyst for methanol synthesis by CO<sub>2</sub> hydrogenation. *Angew. Chem. Int. Ed.* **2016**, *55*, 6261–6265. [[CrossRef](#)] [[PubMed](#)]
23. Wang, J.; Li, G.; Li, Z.; Tang, C.; Feng, Z.; An, H.; Liu, H.; Liu, T.; Li, C. A highly selective and stable ZnO-ZrO<sub>2</sub> solid solution catalyst for CO<sub>2</sub> hydrogenation to methanol. *Sci. Adv.* **2017**, *3*, e1701290. [[CrossRef](#)] [[PubMed](#)]
24. Levy, R.B.; Boudart, M. Platinum-like behavior of tungsten carbide in surface catalysis. *Sci. New Ser.* **1973**, *181*, 547–549. [[CrossRef](#)] [[PubMed](#)]
25. Ma, F.; Wu, H.B.; Xia, B.Y.; Xu, C.; Lou, X.W. Hierarchical β-Mo<sub>2</sub>C nanotubes organized by ultrathin nanosheets as a highly efficient electrocatalyst for hydrogen production. *Angew. Chem. Int. Ed.* **2015**, *54*, 15395–15399. [[CrossRef](#)] [[PubMed](#)]
26. Akmach, D.; Bathla, S.; Tran, C.C.; Kaliaguine, S.; Mushrif, S.H. Transition metal carbide catalysts for Upgrading lignocellulosic biomass-derived oxygenates: A review of the experimental and computational investigations into structure-property relationships. *Catal. Today* **2023**, *423*, 114285. [[CrossRef](#)]
27. Jujuri, S.; Cárdenas-Lizana, F.; Keane, M.A. Synthesis of group VI carbides and nitrides: Application in catalytic hydrodechlorination. *J. Mater. Sci.* **2014**, *49*, 5406–5417. [[CrossRef](#)]
28. Qiu, Z.; Wang, Y.; Li, Z.; Cao, Y.; Li, Q. Hydrodenitrogenation of Quinoline with high selectivity to aromatics over α-MoC<sub>1-x</sub>. *Mol. Catal.* **2021**, *516*, 112002. [[CrossRef](#)]
29. Dubois, J.-L.; Sayama, K.; Arakawa, H. CO<sub>2</sub> hydrogenation over carbide catalysts. *Chem. Lett.* **1992**, *21*, 5–8. [[CrossRef](#)]
30. Posada-Pérez, S.; Viñes, F.; Ramirez, P.J.; Vidal, A.B.; Rodriguez, J.A.; Illas, F. The bending machine: CO<sub>2</sub> activation and hydrogenation on δ-MoC(001) and β-Mo<sub>2</sub>C(001) surfaces. *Phys. Chem. Chem. Phys.* **2014**, *16*, 14912–14921. [[CrossRef](#)]
31. Han, H.; Cui, P.; Xiao, L.; Wu, W. MoCS@NSC with interfacial heterostructure nanostructure: A highly selective catalyst for synthesizing methanol from CO<sub>2</sub> at low temperature. *J. Environ. Chem. Eng.* **2021**, *9*, 106354. [[CrossRef](#)]
32. Hu, J.; Yu, L.; Deng, J.; Wang, Y.; Cheng, K.; Ma, C.; Zhang, Q.; Wen, W.; Yu, S.; Pan, Y.; et al. Sulfur vacancy-rich MoS<sub>2</sub> as a catalyst for the hydrogenation of CO<sub>2</sub> to methanol. *Nat. Catal.* **2021**, *4*, 242–250. [[CrossRef](#)]
33. Sharma, M.D.; Mahala, C.; Basu, M. 2D thin sheet heterostructures of MoS<sub>2</sub> on MoSe<sub>2</sub> as efficient electrocatalyst for hydrogen evolution reaction in wide pH range. *Inorg. Chem.* **2020**, *59*, 4377–4388. [[CrossRef](#)] [[PubMed](#)]
34. Wazir, M.B.; Daud, M.; Safeer, S.; Almarzooqi, F.; Qurashi, A. Review on 2D molybdenum diselenide (MoSe<sub>2</sub>) and its hybrids for green hydrogen (H<sub>2</sub>) generation applications. *ACS Omega* **2022**, *7*, 16856–16865. [[CrossRef](#)] [[PubMed](#)]
35. Xu, J.; Li, X.; Liu, W.; Sun, Y.; Ju, Z.; Yao, T.; Wang, C.; Ju, H.; Zhu, J.; Wei, S.; et al. Carbon Dioxide electroreduction into syngas boosted by a partially delocalized charge in molybdenum sulfide selenide alloy monolayers. *Angew. Chem. Int. Ed.* **2019**, *56*, 9121–9125. [[CrossRef](#)] [[PubMed](#)]
36. Qu, H.; He, S.; Su, Y.; Zhang, Y.; Su, H. MoSe<sub>2</sub>: A promising non-noble metal catalyst for direct ethanol synthesis from syngas. *Fuel* **2020**, *281*, 118760. [[CrossRef](#)]
37. Zhao, G.-Q.; Long, X.; Zou, J.; Hu, J.; Jiao, F.-P. Design of hollow nanostructured photocatalysts for clean energy production. *Coord. Chem. Rev.* **2023**, *477*, 214953. [[CrossRef](#)]
38. Dai, M.; Wang, R. Synthesis and applications of nanostructured hollow transition metal chalcogenides. *Small* **2021**, *17*, 2006813. [[CrossRef](#)] [[PubMed](#)]
39. Liu, Y.; Zhu, M.; Chen, D. Sheet-like MoSe<sub>2</sub>/C composites with enhanced Li-ion storage properties. *J. Mater. Chem. A* **2015**, *3*, 11857–11862. [[CrossRef](#)]
40. Zhang, X.; Xiong, Y.; Dong, M.; Hou, Z.; Qian, Y. Construction of hierarchical MoSe<sub>2</sub>@C hollow nanospheres for efficient lithium/sodium ion storage. *Inorg. Chem. Front.* **2020**, *7*, 1691–1698. [[CrossRef](#)]
41. Liu, H.; Liu, B.; Guo, H.; Liang, M.; Zhang, Y.; Borjigin, T.; Yang, X.; Wang, L.; Sun, X. N-doped C-encapsulated scale-like yolk-shell frame assembled by expanded planes few-layer MoSe<sub>2</sub> for enhanced performance in sodium-ion batteries. *Nano Energy* **2018**, *51*, 639–648. [[CrossRef](#)]
42. Tang, H.; Dou, K.; Kaun, C.C.; Kuang, Q.; Yang, S. MoSe<sub>2</sub> nanosheets and their graphene hybrids: Synthesis, characterization and hydrogen evolution reaction studies. *J. Mater. Chem. A* **2014**, *2*, 360–364. [[CrossRef](#)]
43. Guan, D.; Shi, C.; Xu, H.; Gu, Y.; Zhong, J.; Sha, Y.; Shao, Z. Simultaneously mastering operando strain and reconstruction effects via phase-segregation strategy for enhanced oxygen-evolving electrocatalysis. *J. Energy Chem.* **2023**, *82*, 572–580. [[CrossRef](#)]
44. Chen, B.; Meng, Y.; He, F.; Liu, E.; Shi, C.; He, C.; Ma, L.; Li, Q.; Li, J.; Zhao, N. Thermal decomposition-reduced layer-by-layer nitrogen-doped graphene/MoS<sub>2</sub>/nitrogen-doped graphene heterostructure for promising lithium-ion batteries. *Nano Energy* **2017**, *41*, 154–163. [[CrossRef](#)]
45. Niu, F.; Yang, J.; Wang, N.; Zhang, D.; Fan, W.; Yang, J.; Qian, Y. MoSe<sub>2</sub>-covered n, p-doped carbon nanosheets as a long-life and high-rate anode material for sodium-ion batteries. *Adv. Funct. Mater.* **2017**, *27*, 1700522. [[CrossRef](#)]
46. Balati, A.; Bazilio, A.; Shahriar, A.; Nash, K.; Shipley, H.J. Simultaneous formation of ultra-thin MoSe<sub>2</sub> nanosheets, inorganic fullerene-like MoSe<sub>2</sub> and MoO<sub>3</sub> quantum dots using fast and ecofriendly pulsed laser ablation in liquid followed by microwave treatment. *Mater. Sci. Semicond. Process.* **2019**, *99*, 68–77. [[CrossRef](#)]

47. Qu, B.; Li, C.; Zhu, C.; Wang, S.; Zhang, X.; Chen, Y. Growth of MoSe<sub>2</sub> nanosheets with small size and expanded spaces of (002) plane on the surfaces of porous N-doped carbon nanotubes for hydrogen production. *Nanoscale* **2016**, *8*, 16886–16893. [[CrossRef](#)] [[PubMed](#)]
48. Vikraman, D.; Hussain, S.; Karuppasamy, K.; Feroze, A.; Kathalingam, A.; Sanmugam, A.; Chun, S.H.; Jung, J.; Kim, H.S. Engineering the novel MoSe<sub>2</sub>-Mo<sub>2</sub>C hybrid nanoarray electrodes for energy storage and water splitting applications. *Appl. Catal. B Environ.* **2020**, *264*, 118531. [[CrossRef](#)]
49. Ge, P.; Hou, H.; Banks, C.E.; Foster, C.W.; Li, S.; Zhang, Y.; He, J.; Zhang, C.; Ji, X. Binding MoSe<sub>2</sub> with carbon constrained in carbonous nanosphere towards high-capacity and ultrafast Li/Na-ion storage. *Energy Storage Mater.* **2018**, *12*, 310–323. [[CrossRef](#)]
50. Liu, H.; Guo, H.; Liu, B.; Liang, M.; Lv, Z.; Adair, K.R.; Sun, X. Few-layer MoSe<sub>2</sub> nanosheets with expanded (002) planes confined in hollow carbon nanospheres for ultrahigh-performance Na-ion batteries. *Adv. Funct. Mater.* **2018**, *28*, 1707480. [[CrossRef](#)]
51. Li, J.; Hong, W.; Jian, C.; Cai, Q.; He, X.; Liu, W. High-performance hydrogen evolution at a MoSe<sub>2</sub>-Mo<sub>2</sub>C seamless heterostructure enabled by efficient charge transfer. *J. Mater. Chem. A* **2020**, *8*, 6692–6698. [[CrossRef](#)]
52. Su, J.; Nie, Z.; Feng, Y.; Hu, X.; Li, H.; Zhao, Z.; Zan, S.; Qi, S. Hollow core-shell structure Co/C@MoSe<sub>2</sub> composites for high-performance microwave absorption. *Compos. Part A Appl. Sci. Manuf.* **2022**, *162*, 107140. [[CrossRef](#)]
53. Tang, J.; Huang, C.; Wu, Q.; Cui, A.; Li, W. Atomic-scale intercalation of N-doped carbon into monolayered MoSe<sub>2</sub>-Mo<sub>2</sub>C heterostructure as a highly efficiency hydrogen evolution reaction catalyst. *J. Electroanal. Chem.* **2022**, *906*, 115897. [[CrossRef](#)]
54. Zhang, L.; Cao, X.; Feng, C.; Zhang, W.; Wang, Z.; Feng, S.; Huang, Z.; Lu, X.; Dai, F. Interfacial Mo-N-C bond endowed hydrogen evolution reaction on MoSe<sub>2</sub>@N-Doped carbon hollow nanoflowers. *Inorg. Chem.* **2021**, *60*, 12377–12385. [[CrossRef](#)] [[PubMed](#)]
55. Huang, H.; Cui, J.; Liu, G.; Bi, R.; Zhang, L. Carbon-coated MoSe<sub>2</sub>/MXene hybrid nanosheets for superior potassium storage. *ACS Nano* **2019**, *13*, 3448–3456. [[CrossRef](#)] [[PubMed](#)]
56. Zhang, H.; Guan, D.; Gu, Y.; Xu, H.; Wang, C.; Shao, Z.; Guo, Y. Tuning synergy between nickel and iron in Ruddlesden-Popper perovskites through controllable crystal dimensionalities towards enhanced oxygen-evolving activity and stability. *Carbon Energy* **2024**, *6*, e465. [[CrossRef](#)]
57. Zhang, Y.; He, Y.; Cao, M.; Liu, B.; Li, J. High selective methanol synthesis from CO<sub>2</sub> hydrogenation over Mo-Co-C-N catalyst. *Fuel* **2022**, *325*, 124854. [[CrossRef](#)]
58. Ma, Z.-Y.; Yang, C.; Wei, W.; Li, W.-H.; Sun, Y.-H. Surface properties and CO adsorption on zirconia polymorphs. *J. Mol. Catal. A Chem.* **2005**, *227*, 119–124. [[CrossRef](#)]
59. Dong, X.; Li, F.; Zhao, N.; Xiao, F.; Wang, J.; Tan, Y. CO<sub>2</sub> hydrogenation to methanol over Cu/ZnO/ZrO<sub>2</sub> catalysts prepared by precipitation-reduction method. *Appl. Catal. B Environ.* **2016**, *191*, 8–17. [[CrossRef](#)]
60. Zhou, Y.; Liu, F.; Geng, S.; Yao, M.; Ma, J.; Cao, J. Tuning the content of S vacancies in MoS<sub>2</sub> by Cu doping for enhancing catalytic hydrogenation of CO<sub>2</sub> to methanol. *Mol. Catal.* **2023**, *547*, 113288. [[CrossRef](#)]
61. Yang, Z.; He, Y.; Tang, P.; Xu, C.; Zhang, G.; He, J. Oxygen-incorporated 3D flower-like MoS<sub>2</sub> microsphere as a bifunctional catalyst for effective synthesis of 2,5-diformylfuran from fructose. *Catal. Sci. Technol.* **2023**, *13*, 2340–2348. [[CrossRef](#)]
62. Zhang, P.; Na, W.; Zuo, J.; Wen, J.; Huang, Z.; Huang, H.; Gao, W.; Qi, X.; Zheng, M.; Wang, H. CO<sub>2</sub> hydrogenation to methanol over hydrothermally synthesized Inx-Zry catalysts. *Mol. Catal.* **2023**, *538*, 112977. [[CrossRef](#)]
63. Heracleous, E.; Koidi, V.; Lappas, A.A. Experimental Investigation of Sorption-Enhanced CO<sub>2</sub> Hydrogenation to Methanol. *ACS Sustain. Chem. Eng.* **2023**, *11*, 9684–9695.
64. Wei, Y.; Liu, F.; Ma, J.; Yang, C.; Wang, X.; Cao, J. Catalytic roles of In<sub>2</sub>O<sub>3</sub> in ZrO<sub>2</sub>-based binary oxides for CO<sub>2</sub> hydrogenation to methanol. *Mol. Catal.* **2022**, *525*, 112354. [[CrossRef](#)]
65. Daifeng, L.; Zhen, Z.; Yinye, C.; Lingxing, Z.; Xiaochuan, C.; Xuhui, Y.; Baoquan, H.; Yongjin, L.; Qingrong, Q.; Qinghua, C. The Co-In<sub>2</sub>O<sub>3</sub> interaction concerning the effect of amorphous Co metal on CO<sub>2</sub> hydrogenation to methanol. *J. CO<sub>2</sub> Util.* **2022**, *65*, 102209. [[CrossRef](#)]
66. Rasteiro, L.F.; De Sousa, R.A.; Vieira, L.H.; Ocampo-Restrepo, V.K.; Verga, L.G.; Assaf, J.M.; Da Silva, J.L.F.; Assaf, E.M. Insights into the alloy-support synergistic effects for the CO<sub>2</sub> hydrogenation towards methanol on oxide-supported Ni<sub>5</sub>Ga<sub>3</sub> catalysts: An experimental and DFT study. *Appl. Catal. B Environ.* **2022**, *302*, 120842. [[CrossRef](#)]
67. Alabsi, M.H.; Chen, X.; Wang, X.; Zhang, M.; Ramirez, A.; Duan, A.; Xu, C.; Cavallo, L.; Huang, K.W. Highly dispersed Pd nanoparticles supported on dendritic mesoporous CeZrZnO<sub>x</sub> for efficient CO<sub>2</sub> hydrogenation to methanol. *J. Catal.* **2022**, *413*, 751–761. [[CrossRef](#)]
68. Wang, Y.; Yu, H.; Hu, Q.; Huang, Y.; Wang, X.; Wang, Y.; Wang, F. Application of microimpinging stream reactor coupled with ultrasound in Cu/CeZrO<sub>x</sub> solid solution catalyst preparation for CO<sub>2</sub> hydrogenation to methanol. *Renew. Energy* **2023**, *202*, 834–843. [[CrossRef](#)]
69. Zhou, S.; Zeng, H.C. Boxlike Assemblages of few-layer MoS<sub>2</sub> nanosheets with edge blockage for high-efficiency hydrogenation of CO<sub>2</sub> to methanol. *ACS Catal.* **2022**, *12*, 9872–9886. [[CrossRef](#)]
70. Chen, G.; Yu, J.; Li, G.; Zheng, X.; Mao, H.; Mao, D. Cu<sup>+</sup>-ZrO<sub>2</sub> interfacial sites with highly dispersed copper nanoparticles derived from Cu@UiO-67 hybrid for efficient CO<sub>2</sub> hydrogenation to methanol. *Int. J. Hydrogen Energy* **2023**, *48*, 2605–2616. [[CrossRef](#)]
71. Wang, Y.; Zhang, X.; Hong, X.; Liu, G. Sulfate-promoted higher alcohol synthesis from CO<sub>2</sub> hydrogenation. *ACS Sustain. Chem. Eng.* **2022**, *10*, 8980–8987.

72. Marcos, F.C.F.; Alvim, R.S.; Lin, L.; Betancourt, L.E.; Petrolini, D.D.; Senanayake, S.D.; Alves, R.M.B.; Assaf, J.M.; Rodriguez, J.A.; Giudici, R.; et al. The role of copper crystallization and segregation toward enhanced methanol synthesis via CO<sub>2</sub> hydrogenation over CuZrO<sub>2</sub> catalysts: A combined experimental and computational study. *Chem. Eng. J.* **2023**, *452*, 139519. [[CrossRef](#)]
73. Zhou, S.; Kosari, M.; Zeng, H.C. Boosting CO<sub>2</sub> hydrogenation to methanol over monolayer MoS<sub>2</sub> nanotubes by creating more strained basal planes. *J. Am. Chem. Soc.* **2024**, *146*, 10032–10043. [[CrossRef](#)]
74. Zhou, S.; Ma, W.; Anjum, U.; Kosari, M.; Xi, S.; Kozlov, S.M.; Zeng, H.C. Strained few-layer MoS<sub>2</sub> with atomic copper and selectively exposed in-plane sulfur vacancies for CO<sub>2</sub> hydrogenation to methanol. *Nat. Commun.* **2023**, *14*, 5872. [[CrossRef](#)] [[PubMed](#)]
75. Yuan, Y.; Qi, L.; Gao, Z.; Guo, T.; Zhai, D.; He, Y.; Guo, Q. Performance exploration of Ni-doped MoS<sub>2</sub> in CO<sub>2</sub> hydrogenation to methanol. *Molecules* **2023**, *28*, 5796. [[CrossRef](#)] [[PubMed](#)]
76. Zou, R.; Shen, C.; Sun, K.; Ma, X.; Ma, X.; Li, Z.; Li, M.; Liu, C.J. CO<sub>2</sub> hydrogenation to methanol over the copper promoted In<sub>2</sub>O<sub>3</sub> catalyst. *J. Energy. Chem.* **2024**, *93*, 135–145. [[CrossRef](#)]
77. Wang, J.; Song, Y.; Li, J.; Liu, F.; Wang, J.; Lv, J.; Ma, X. Modulation of Al<sub>2</sub>O<sub>3</sub> and ZrO<sub>2</sub> composite in Cu/ZnO-based catalysts with enhanced performance for CO<sub>2</sub> hydrogenation to methanol. *Appl. Catal. A* **2024**, *674*, 119618. [[CrossRef](#)]

**Disclaimer/Publisher's Note:** The statements, opinions and data contained in all publications are solely those of the individual author(s) and contributor(s) and not of MDPI and/or the editor(s). MDPI and/or the editor(s) disclaim responsibility for any injury to people or property resulting from any ideas, methods, instructions or products referred to in the content.